scientific reports

Check for updates

OPEN

Experimental and theoretical evaluation of geometry-dependent doxorubicin loading onto cerium oxide nanoparticles via van der Waals interaction modeling

Panyada Sripaturad[1], Sereysonita Keo[2], Anongnat Wongpan[2], Wiradet Siri[3], Napasorn Tana-atsawapon[2], Patraporn Luksirikul[3,4], Kanlaya Katewongsa[2,6]✉ & Duangkamon Baowan[1,5,6]✉

We employed a combined experimental and analytical approach to investigate the influence of nanoparticle geometry on the loading efficiency of doxorubicin (DOX) onto CeO_2 nanoparticles. Experimentally, three distinct CeO_2 shapes, spherical, sheet, and cylindrical, were synthesized, characterized, and their respective DOX loading efficiencies were measured. Concurrently, analytical mathematical models were developed to calculate the van der Waals (vdW) interaction energy between a spherical DOX molecule and each nanoparticle geometry, considering both theoretical loading and surface adsorption scenarios. The model successfully predicted the relative thermodynamic stability by yielding high and similar binding energies for the spherical and sheet geometries, which aligned well with their high experimental loading efficiencies. However, a significant quantitative discrepancy arose with the cylindrical shape, where the predicted binding energy did not correspond to the high experimental loading efficiency. This divergence powerfully demonstrates that a simple vacuum-based vdW model is fundamentally insufficient to fully capture the complexity of the drug-nanoparticle interaction. Despite this limitation, the synergy between experimental validation and theoretical modeling provides a critical framework for understanding the geometric dependence of drug-nanoparticle interactions and guides future model refinement toward incorporating the complexity of the nano-bio interface.

Nanostructures have been crucial in advancing drug and medical research for decades, establishing the field of nanomedicine. The use of nanoscale materials has led to a wide range of applications in the diagnosis and treatment of various diseases, including kidney[1], cardiovascular[2], and cancer-related diseases[3,4]. Furthermore, several types of nanoparticles have demonstrated the properties such that enhance the efficiency of drug delivery systems in reaching target cells such as liposomes, polymeric and solid lipid nanoparticles[5–13]. Cerium oxide (CeO_2) nanoparticle is also considered as one of the effective carriers in drug delivery, showing remarkable antioxidant properties, antibacterial activity, excellent biocompatibility and the capacity to support wound healing[14–16]. As a result, these properties lead to a powerful potential of CeO_2 in cancer therapy by minimizing toxicity and maximizing killing ability for anticancer drug[13,17,18].

A severe increase in the global incidence of cancer has necessitated the development of numerous advanced therapeutic treatments and pharmacological agents. Doxorubicin (DOX) can be administered more effectively to treat many types of cancer when loaded with nanoparticles. For example, attaching CeO_2 nanoparticles with DOX increases the ability of DOX to fight breast cancer, making them promising new treatments[19].

[1]Department of Mathematics, Faculty of Science, Mahidol University, Bangkok 10400, Thailand. [2]Department of Biochemistry, Faculty of Science, Mahidol University, Bangkok 10400, Thailand. [3]Department of Chemistry, Faculty of Science, Kasetsart University, Bangkok 10900, Thailand. [4]Center for Advanced Studies in Nanotechnology for Chemical, Food and Agricultural Industries, KU Institute for Advanced Studies, Kasetsart University, Bangkok 10900, Thailand. [5]Centre of Excellence in Mathematics, CHE, Si Ayutthaya Rd., Bangkok 10400, Thailand. [6]Kanlaya Katewongsa and Duangkamon Baowan contributed equally to this work. ✉email: kanlaya.pra@mahidol.edu; duangkamon.bao@mahidol.ac.th

Recent advances in nanomedicine have demonstrated that nanoparticle geometry plays a pivotal role in optimizing doxorubicin (DOX) drug loading and delivery. The shape, size, and surface features of nanocarriers such as nonionic surfactant vesicles[20], black phosphorus nanoparticles[21], and DNA origami structures[22] greatly influence DOX encapsulation efficiency, release kinetics, and therapeutic performance. These innovative geometries enable improved targeting, controlled drug release, and enhanced cytotoxicity, emphasizing the importance of geometric tuning and surface engineering for more effective and safer DOX-based cancer therapies. The shape and size of nanoparticles are also vital for their effectiveness[23] so many conformations are studied such as spheres, rods, disks, and cones. The size impact on factors relating to their circulation duration, targeting efficiency, and cellular uptake. In addition, different shapes can influence how cells absorb them and can improve the precision of drug delivery[24,25]. For instant, spherical nanoparticles produce the most favorable outcome in terms of drug adsorption[24] and non-spherical particles such as rods and wormlike particles, possess a higher drug loading capacity[25,26]. Therefore, it is essential to also consider the shape of the nanoparticles to optimize the efficiency of the delivery system.

Recent progress in theoretical modeling has profoundly enhanced our understanding of nanomaterials, primarily through the integration of advanced van der Waals (vdW) corrected Density Functional Theory (DFT) methods[27,28]. These developments include automated algorithms capable of constructing and screening large numbers of bilayer vdW supercells. This capability provides deep insights into how factors like supercell geometry, twist angle, and strain impact electronic and mechanical properties[28], thereby overcoming limitations inherent to conventional DFT when modeling metastable configurations in layered vdW heterostructures. Furthermore, recent reviews underscore the necessity of incorporating long-range dispersion and nonlocal interactions for realistic simulation of nanomaterial architectures, particularly in applications like catalysis, energy devices, and environmental technologies[27]. This necessity highlights that London dispersion interactions are crucial for accurate molecular modeling; explicit consideration of these long-range electron correlations demonstrably improves predictions of molecular stability, reactivity, and material properties. The robust integration of computational and experimental techniques has firmly established dispersion forces as a critical factor in the rational design and comprehensive understanding of modern nanomaterials[29].

Mathematical modeling is another key in developing nanostructure geometries, especially for predicting drug delivery system[30]. The Lennard-Jones potential function is adopted as a tool in finding the interaction energy between two non-bonded atoms which is beneficial for the finding of energy optimization. Several studies use the model to describe the encapsulation capacity of multiple conformations of DOX including sphere, cylinder, and ellipse, for various carriers such as liposome, peptide nanotube, and lipid nanotube[31–33]. Consequently, to improve the efficiency in using CeO_2 as a carrier delivering drug DOX to targeted cells, we investigate the interaction energy, using the Lennard-Jones potential function, between three conformations of CeO_2, which are sphere, planar sheet and cylinder, and a spherical drug DOX.

The current understanding of drug-nanoparticle interactions often relies on either experimental observations or computational simulations. However, a comprehensive study that systematically links a fundamental analytical model with direct experimental validation across various nanoparticle geometries remains largely unexplored. This study addresses this gap by presenting a combined approach to investigate the interaction between a DOX molecule and three distinct CeO_2 nanoparticle shapes. Analytical expressions for the vdW energy are derived for spherical, sheet, and cylindrical geometries and are directly compared with experimental measurements of DOX loading efficiency. This integrated methodology provides a unique synergy, the analytical models offer a theoretical framework that explains the observed experimental trends, while the experimental data validates the models' predictive capabilities. This approach provides a deeper and more complete understanding of how nanoparticle geometry fundamentally influences drug-nanoparticle interactions.

The following sections provide a detailed overview of this study. The experimental details for the synthesis and characterization of different shapes of CeO_2 nanoparticles, along with the measurement of DOX loading efficiency, are described in Section 2. Section 3 presents the mathematical derivation for the non-bonded interaction energy of the molecules. The numerical results from the analytical expressions, including a comparison with our experimental findings, are provided in Section 4. Finally, a summary of the key findings is given in Section 5.

Experimental study

We begin by synthesizing CeO_2 nanoparticles in different shapes and characterizing their morphology using Transmission Electron Microscopy (TEM). Following characterization, we determine the loading efficiency of DOX onto each CeO_2 shape and evaluate the cytotoxicity on breast cancer cells.

Materials

Cerium (III) nitrate hexahydrate; $Ce(NO_3)_3{\cdot}6H_2O$ 99% (Sigma Aldrich), sodium hydroxide anhydrous; NaOH $\geq 98\%$ (Carlo Erba), ethylene glycol; $CH_2\ OHCH_2OH \geq 99.5\%$ (Sigma Aldrich), ethyl alcohol; $C_2\ H_5OH$ 99.9% (Duksan), acetic acid; $CH_3COOH > 99.9\%$ (Carlo Erba); dimethyl sulfoxide (DMSO) and 3-(4,5-dimethylthiazol-2-yl)-2,5-diphenyltetrazolium bromide (MTT) (Sigma-Aldrich); Doxorubicin hydrochloride (Thermo Fisher Scientific); Dulbecco's Modified Eagle Medium (DMEM) (Thermo Fisher Scientific); Penicillin-streptomycin (Pen-strep, P/S) (Gibco).

Synthesis of different shapes of CeO_2

Synthesis CeO_2 nanosphere (C-sphere)

CeO_2 nanosphere were synthesized based on the previous protocol with minor modification[34]. Briefly, 2.8092 g of $Ce(NO_3)_3{\cdot}6H_2O$ was dispersed in a mixed solvent consisting of water (2.8 mL), acetic acid (2.8 mL), and ethylene glycol (70 mL). The solution was stirred using a magnetic stirrer for 30 minutes to ensure homogeneity.

The resulting mixture was transferred into a stainless-steel autoclave and subjected to a solvothermal reaction at 180°C for 200 minutes. After cooling to room temperature, the precipitate was collected via centrifugation at 19,319 × g for 10 minutes at 25°C. The pellet was washed five times with 35 mL of deionized water until the pH reached pure deionized water, followed by three washes with 35 mL of ethanol. The resulting solid was dried in a hot air oven at 80°C for 12 hours and then calcined at 400°C for 4 hours in a muffle furnace (a heating rate of 2°C/min). The final product was weighed, and the yield was calculated.

Synthesis CeO_2 nanorods (C-cylinder)
CeO_2 nanorods were synthesized following previously reported methods with minor modifications[35]. 0.8680 g of $Ce(NO_3)_3{\cdot}6H_2O$ was dissolved in 30 mL of 6 M NaOH under magnetic stirring for 30 minutes, resulting in a milky white suspension. The mixture was transferred into a stainless steel autoclave and subjected to a solvothermal treatment at 100°C for 24 hours. After the reaction, the suspension was centrifuged at 19,319 × g for 15 minutes at 25°C. The resulting precipitate was washed five times with 35 mL of deionized water until neutral pH (∼ 7), followed by three ethanol washes (35 mL each). The obtained solid was then dried at 60°C for 24 hours and subsequently calcined at 400°C for 4 hours. The product was weighed to determined yield.

Synthesis CeO_2 sheet-shaped (C-sheet)
CeO_2 nanosheets were synthesize following previously established procedures with minor modifications[36]. $Ce(NO_3)_3{\cdot}6H_2O$ was dissolved in ultrapure water and heated at 50°C on a hot plate with magnetic stirring for 20 minutes. The pH of the solution was adjusted to 12 using NaOH. The mixture was stirred continuously stirrer at 50°C for 24 hours. The resulting nanoparticles were collected via centrifugation at 15,090 × g for 30 minutes and washed with deionized water and ethanol until the supernatant reached neutral pH (∼ 7). The nanoparticles were then freezing dried for 25 hours, and subsequently calcined at 400°C for 2 hours in a muffle furnace. The sheet-shaped cerium oxide nanoparticles were collected and stored for further use.

Transmission electron microscopy (TEM)
TEM images were obtained by JEOL model JEM-2010 TEM operating at 120-200 kV.

Dynamic light scattering analysis (DLS)
The hydrodynamic diameter of the synthesized nanoparticles was measured using a Zetasizer Ultra (Malvern Panalytical) based on the principles of DLS. All measurements were performed at a controlled temperature of 25°C. Prior to analysis, nanoparticle suspensions were diluted 1:100 in deionized water to a final concentration of 0.1 mg/mL, ensuring minimal multiple scattering and optimal accuracy.

Morphological characterization of CeO_2

CeO_2 nanoparticles were synthesized using a hydrothermal method to obtain distinct morphologies. TEM was employed to characterize the spherical, cylindrical, and sheet shaped structures of CeO_2, as shown in Fig. 1. The spherical CeO_2 nanoparticles (C-sphere, Fig. 1(a)) exhibited uniform size distribution with well-defined geometry, and quantitative analysis revealed an average diameter of 204.95 ± 34.91 nm. The cylinder-shaped CeO_2 nanoparticles (C-cylinder, Fig. 1(b)) appeared as elongated particles often forming aggregated networks, with an average length of 86.30 ± 21.84 nm and width of 7.07 ± 2.38 nm, corresponding to an aspect ratio of $\backsim 5.8$. The sheet-like CeO_2 (C-sheet, Fig. 1(c)) displayed a transparent, thin, and layered morphology with partial aggregation into overlapping structures, consistent with their two-dimensional nature; size analysis showed an average lateral dimension of 263.34 ± 202.04 nm and width of 84.74 ± 33.26 nm. The total number of measured particles ($n = 34$) represents the overall morphology and size uniformity across samples. The averaged size are reported as mean ± SEM. Additionally, the TEM size distribution histograms for all three CeO_2 nanoparticle morphologies are provided in Supplementary Figure S1. The size distribution

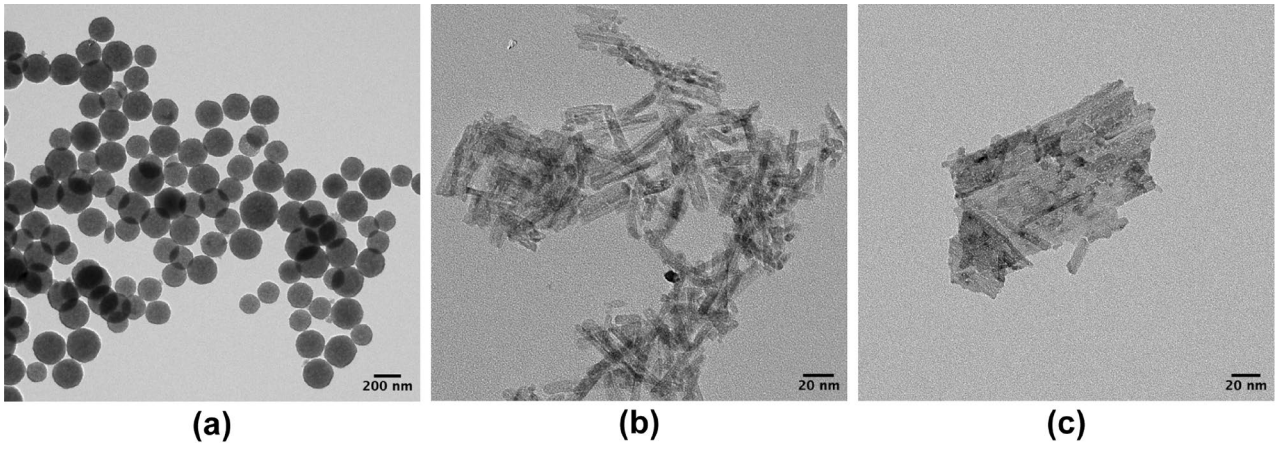

Fig. 1. The microscope image from TEM technique includes (**a**) C-sphere with scale bar = 200 nm, (**b**) C-cylinder, and (**c**) C-sheet with scale bar = 20 nm.

histograms further confirmed consistent particle formation with minor variations among morphologies. These results confirm successful synthesis of CeO_2 nanoparticles with morphology-controlled structures, which may critically influence their physicochemical properties and subsequent biological or catalytic activities.

DOX loaded on different shapes of CeO_2

Three different shapes of CeO_2 nanoparticles were dispersed in PBS at a concentration of 1 mg/mL by stirring for 15 minutes. Separately, 500 μM of DOX was was added to 200 μL of 1 mg/mL CeO_2 nanoparticles in $1\times$ PBS, and the mixture was vortexed. The two solutions were combined and stirred in the dark for $16-18$ hours. After incubation, the mixture was subjected to ultracentrifugation at 15,000 $\times$ g for 10 minutes using a Multifuge X Pro Series ultracentrifuge (Thermo Scientific). The resulting cell pellet, representing the DOX-loaded CeO_2 nanoparticles, was collected, dried at 50°C, and stored at room temperature. All experiments were performed in triplicate ($n = 3$) to ensure reproducibility. The supernatant was collected and analysed for loading efficiency (%LE) using a UV-Vis Spectrophotometer (Shimadzu) over a wavelength range of $270-600$ nm. The blank correction procedure, performed by subtracting the absorbance of the corresponding solvent control. The determination is based on quantifying the unabsorbed DOX in the supernatant at an absorbance maximum of 480 nm, according to the equations:

$$\%\text{LE} = \frac{\text{Total drug} - \text{Unabsorbed drug}}{\text{Amount of drug}} \times 100.$$

The optical properties of CeO_2 nanoparticles and their DOX-loaded nanoparticles (CeO_2 NPs–DOX) were investigated to assess morphology-dependent drug-loading behavior. In Fig. 2(a), UV–vis spectra of bare CeO_2 nanoparticles showed a characteristic absorption peak around 320 nm, with no observable DOX absorbance at 480 nm, indicating the absence of free drug across all nanoparticle shapes.

To evaluate %LE, the supernatant collected after DOX loading was analyzed. Representative UV–Vis spectra of DOX solutions and the corresponding blank are provided in Supplementary Figure S2. UV–Vis spectra of the supernatants clearly showed the characteristic DOX absorbance peak, and decreasing intensity across different nanoparticle morphologies indicated varying amounts of drug uptake as shown in Fig. 2(b). These results confirmed the successful loading of DOX into all three nanoparticle morphologies. The UV–Vis calibration

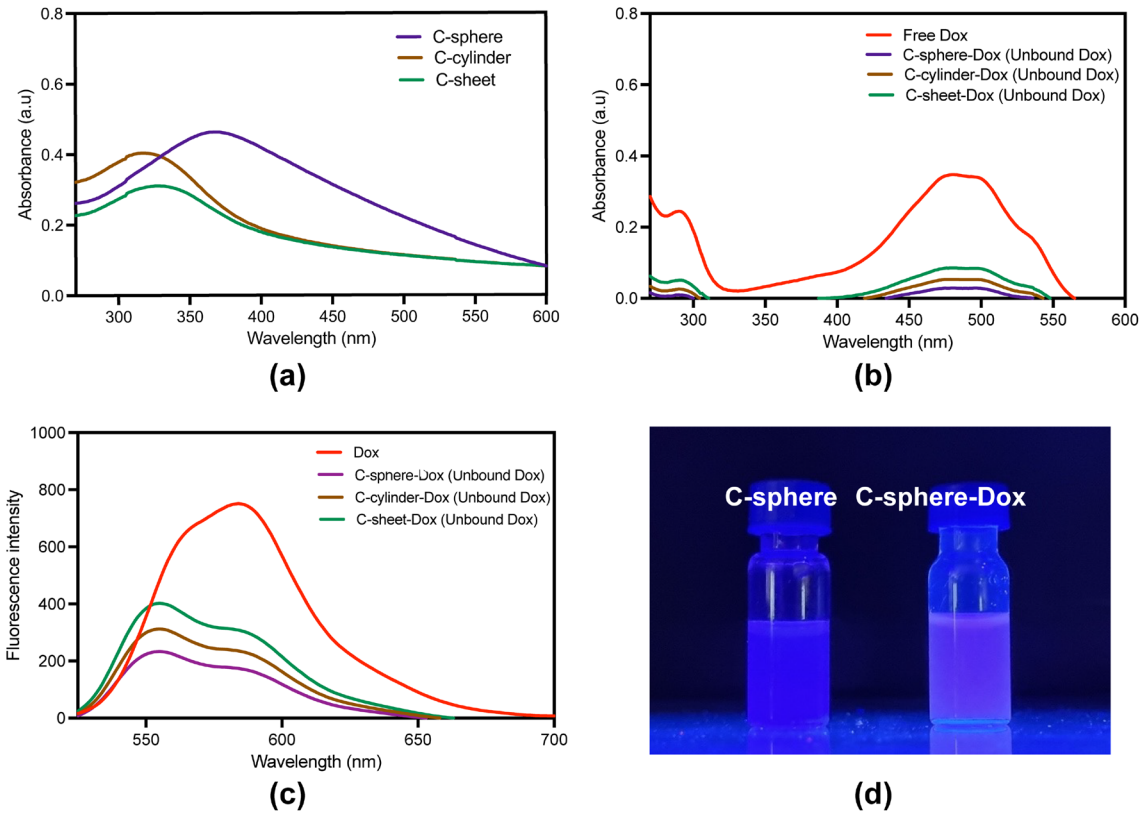

Fig. 2. UV–vis absorption and fluorescence spectral analysis of CeO_2 and CeO_2 NPs-DOX with different morphologies. (**a**) UV–vis of bare CeO_2, (**b**) UV–vis and (**c**) fluorescence emission spectra of supernatants after incubation with DOX for different CeO_2 morphologies. The absorbance corresponds to unbound DOX, decreased peak intensity indicates greater drug uptake by the nanoparticles. (**d**) Visual confirmation of DOX loading under UV illumination. DOX emitted fluorescence, confirming the successful loading of DOX onto the CeO_2.

curve of DOX was constructed, showing excellent linearity ($R^2 = 0.999$). Limit of detection (LOD) and limit of quantification (LOQ) for DOX were calculated from the calibration line using the equations LOD = 3.3× SD/slope and LOQ = 10× SD/slope, as previously reported[37]. Based on the standard deviation of the blank and the slope of the calibration curve, the LOD and LOQ were determined to be 2.83 and 8.57, respectively. The %LE were calculated from the difference between the initial and remaining DOX concentrations. The loading efficiency values are reported as mean ± SEM from three independent experiments ($n = 3$). Among the various morphologies of CeO_2 nanoparticles, C-sphere-DOX exhibited the highest loading efficiency ($85.86 \pm 0.56\%$), followed by C-cylinder-DOX ($78.58 \pm 0.66\%$) and C-sheet-DOX ($67.47 \pm 2.74\%$) (see Table 1). The hydrodynamic sizes of CeO_2 NPs-DOX were measured using DLS and are summarized in Table 1. The percent loading efficiency of C-sphere-DOX and C-cylinder-DOX was significantly higher than that of C-sheet-DOX ($p < 0.001$ and $p < 0.01$, respectively), as determined by one-way ANOVA followed by Tukey's multiple comparison test.

Among the different shapes, C-sheet-DOX exhibited the largest particle size, likely due to greater aggregation tendencies in aqueous solution, followed by C-cylinder-DOX, whereas C-sphere-DOX showed the smallest size. DLS measurements were conducted in water and in PBS. A fluorescence spectrum of unbound DOX in supernatant of DOX-loaded CeO_2 nanoparticles further supported drug loading: C-sphere–DOX showed the lowest DOX fluorescence intensity, indicating minimal unbound drug and effective loading as shown in Fig. 2(c).

The visual confirmation of drug loading was obtained under UV illumination as presented in Fig. 2(d). While bare C-sphere suspension showed negligible fluorescence (left), C-sphere-DOX suspension exhibited a clear fluorescence detectable by the naked eye, confirming successful DOX loading onto CeO_2 particles (right). Overall, these results demonstrate that the shapes of CeO_2 nanoparticles significantly affects their optical behavior and drug-loading performance of CeO_2 nanoparticles based delivery systems.

In vitro evaluation of anticancer effects of DOX loaded CeO_2 on breast cancer cells

The cytotoxicity of free DOX, bare CeO_2, and DOX-loaded CeO_2 nanoparticles with different shapes was evaluated in MDA-MB-231 breast cancer cells using the MTT assay. The percent cell viability of each bare CeO_2 morphology and DOX-loaded CeO_2 was compared in Fig. 3 using the same concentration of nanoparticles, while the cytotoxicity profile of free DOX was provided in the Supplementary Figure S3. Among the bare nanoparticles, C-sphere exhibited the highest cytotoxicity with an IC_{50} of 324.50 ± 49.82 μg/mL, whereas C-cylinder and C-sheet CeO_2 did not reach IC_{50} within the tested concentration range, indicating low toxicity. DOX-loaded CeO_2 exhibited greater cytotoxicity than bare CeO_2. Among the shapes tested, C-sphere-DOX exhibited the lowest IC_{50} (21.95 ± 2.28 μg/mL), followed by C-cylinder-DOX (33.78 ± 2.78 μg/mL) and C-sheet-DOX (87.8 ± 9.44 μg/mL) as shown in Table 2, indicating superior drug delivery efficiency. Notably, the potent cytotoxicity of C-sphere-DOX correlated with its highest loading efficiency, suggesting that nanoparticle shape plays a critical role in drug loading and therapeutic efficacy, with C-sphere-DOX being the most effective formulation for breast cancer treatment.

In vitro drug release of DOX was investigated using PBS (pH 7.4) to simulate the internal environment. Briefly, 2 mg of DOX-loaded nanoparticles were suspended in 1 mL of PBS and placed in a dialysis membrane (MW cutoff $12,000 - 14,000$ Da) with moderate stirring (120 rpm) at 37°C. At predetermined time points, 1 mL of release medium was collected and immediately replaced with fresh PBS. Released DOX was quantified using a spectrofluorometer (Jasco) at an excitation of 493 nm and emission of 590 nm, and release percentage was calculated as

$$\text{Drug release percentage } (\%) = \frac{\text{Weight fo NPs release each time point}}{\text{Loaded NPs}} \times 100.$$

The cumulative release of DOX exhibited a time-dependent profile (Supplementary Figure S4). Free DOX showed a rapid burst (~ 6% at 1 h), gradually reaching ~ 23% at 24 h and plateauing up to 72 h. In contrast, DOX release from CeO_2 nanocarriers was slower and morphology-dependent: C-sheet-DOX reached ~ 4.3 % at 72 h, C-cylinder-DOX ~ 1.3%, and C-sphere-DOX ~ 0.1%, indicating strong drug retention in compact particles. Loading within CeO_2 reduced burst release and prolonged drug release. Interestingly, the trend in

Sample	Size (nm)	PdI	Zeta potential (mV)	Loading efficiency (%)
C-sphere*	316.2 ± 3.5	0.33 ± 0.04	-8.38	–
C-cylinder*	387.9 ± 49.5	0.54 ± 0.06	-1.38	–
C-sheet*	436.7 ± 92.9	0.48 ± 0.07	-2.30	–
C-sphere-DOX**	480.4 ± 268.0	0.56 ± 0.17	-12.58	$85.86 \pm 0.56^{***}$
C-cylinder-DOX**	986.2 ± 276.9	0.77 ± 0.23	-22.97	$78.58 \pm 0.66^{\#\#}$
C-sheet-DOX**	573.1 ± 23.3	0.33 ± 0.05	-22.93	67.47 ± 2.74

Table 1. Characterization of cerium oxide nanoparticles with and without doxorubicin. Data are presented as mean ± SEM from three independent experiments ($n = 3$). NPs were dispersed in * water solution, ** PBS solution. Statistical analysis was performed using one-way ANOVA followed by Tukey's multiple comparison test. $^{***}p < 0.001$ (C-sphere-DOX vs C-sheet-DOX); $^{\#\#}p < 0.01$ (C-cylinder-DOX vs C-sheet-DOX).

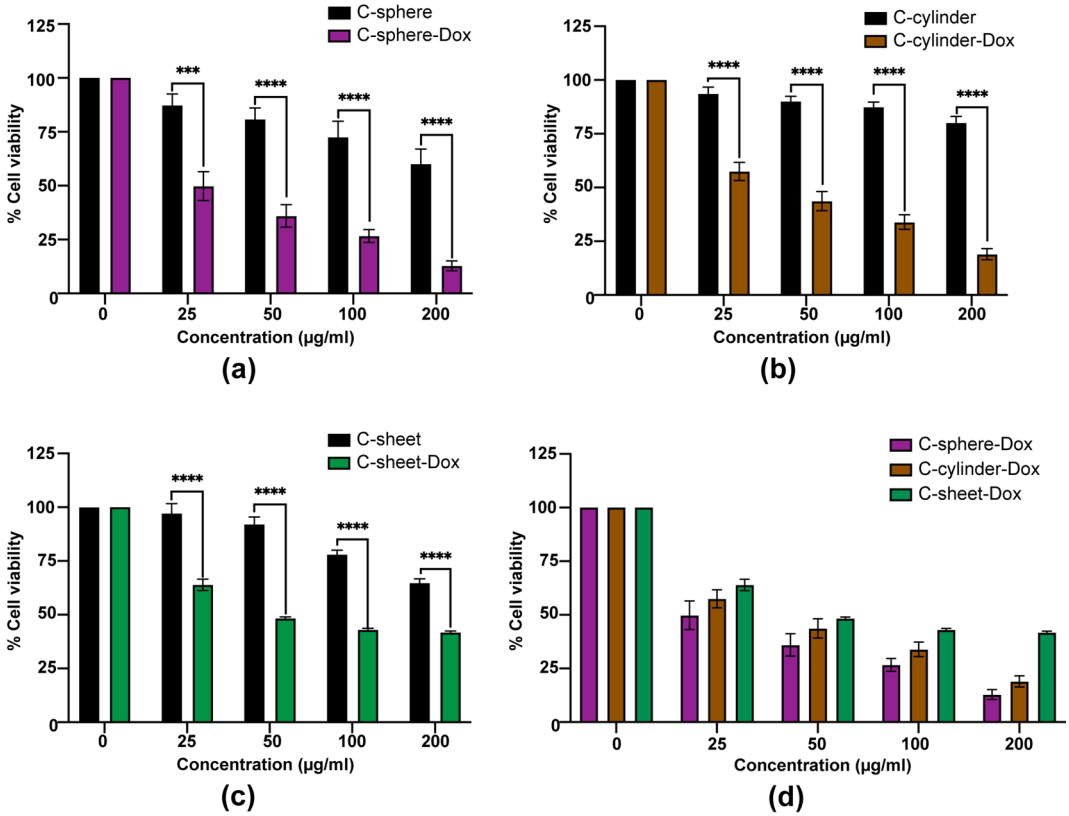

Fig. 3. The cytotoxicity of bare CeO_2 compared to DOX-loaded CeO_2 NPs on MDA-MB-231 cells. (**a**) C-sphere and C-sphere-DOX, (**b**) C-cylinder and C-cylinder-DOX, (**c**) C-sheet and C-sheet-DOX, and (**d**) All DOX-loaded CeO_2 NPs. Data are expressed as mean ± standard error of the mean ($n = 3$). $**p < 0.01$, $***p < 0.001$, and $****p < 0.0001$; Student's T-test.

	IC_{50} (μg/mL)		
	C-sphere	**C-cylinder**	**C-sheet**
Bare NPs	324.50 ± 49.82	N/A	N/A
Loading with DOX	21.95 ± 2.28	33.78 ± 2.78	87.80 ± 9.44

Table 2. The IC_{50} of bare CeO_2 and DOX-loaded CeO_2 with different shapes in MDA-MB-231 cells. N/A (not applicable).

release kinetics (C-sheet > C-cylinder > C-sphere) inversely correlated with cytotoxicity (C-sphere > C-cylinder > C-sheet), suggesting that slower release from highly loaded, compact nanoparticles promotes prolonged intracellular retention of DOX, enhancing cell killing despite lower cumulative release.

Interaction energy between DOX and CeO_2

In order to determine the capacity of delivering DOX to targeted cell, we assume that DOX is modeled as a sphere of radius *a* interacting with the three conformations of CeO_2 surfaces including spherical shape, planar sheet, and cylindrical shape. The Lennard-Jones potential function is utilized to evaluate the interaction energy between two non-bonded atoms, and it is given by

$$E(\rho) = \eta_1 \eta_2 \int_{S_1} \int_{S_2} \left(-\frac{A}{\rho^6} + \frac{B}{\rho^{12}} \right) dS_1 dS_2, \tag{1}$$

where η_1 and η_2 are mean atomic densities of two structures, ρ is a distance between atoms and $A = 2\epsilon\sigma^6$ and $B = \epsilon\sigma^{12}$ are the attractive and repulsive constants, respectively. The values of $\epsilon = \sqrt{\epsilon_1 \epsilon_2}$ is the well-depth and $\sigma = (\sigma_1 + \sigma_2)/2$ is the van der Waals diameter of surface S_1 and S_2 and they are taken from the work of Rappe et al.[38].

The Lennard-Jones constants A and B in the continuous approach may be determined by the weighted average proportional to the atomic types of the two interacting molecules. For example, the constants for the interaction between DOX ($C_{27}\ H_{29}\ NO_{11}$) and CeO_2 sheet are given by

$$\begin{aligned} A =& \frac{1}{3}\left(\frac{27}{68}A_{Ce,C} + \frac{29}{68}A_{Ce,H} + \frac{1}{68}A_{Ce,N} + \frac{11}{68}A_{Ce,O}\right) + \frac{2}{3}\left(\frac{27}{68}A_{O,C} + \frac{29}{68}A_{O,H} + \frac{1}{68}A_{O,N} + \frac{11}{68}A_{O,O}\right) \\ =& 2.0029 \times 10^{-4}\ kcal \cdot mol^{-1} \cdot nm^{6}, \\ B =& \frac{1}{3}\left(\frac{27}{68}B_{Ce,C} + \frac{29}{68}B_{Ce,H} + \frac{1}{68}B_{Ce,N} + \frac{11}{68}B_{Ce,O}\right) + \frac{2}{3}\left(\frac{27}{68}B_{O,C} + \frac{29}{68}B_{O,H} + \frac{1}{68}B_{O,N} + \frac{11}{68}B_{O,O}\right) \\ =& 2.1189 \times 10^{-7}\ kcal \cdot mol^{-1} \cdot nm^{12}, \end{aligned}$$

where DOX has a total of 68 atoms in a molecule. The fractions 1/3 and 2/3 represent the percentage mixing between cerium and oxygen in CeO_2.

We first determine vdW energy between a spherical molecule and an atom as depicted in Fig. 4. For more convenience, we define

$$I_n = \int_{S_1} \rho^{-2n} dS_1, \tag{2}$$

where $n = 3$ and $n = 6$, so the interaction energy of a sphere interacting with a point becomes $E(\rho) = \eta_1\eta_2[-AI_3(\rho) + BI_6(\rho)]$.

The spherical DOX of radius a is assumed to be centered at the origin with its surface element $(a\sin\theta\cos\phi, a\sin\theta\sin\phi, a\cos\theta)$, and the atom is assumed to be located at $(0, 0, \delta)$. Then the square of the Euclidean distance between the surface of the DOX and the atom is given by

$$\rho_{sd}^2 = (a\sin\theta\cos\phi)^2 + (a\sin\theta\sin\phi)^2 + (a\cos\theta - \delta)^2 = a^2 + \delta^2 - 2a\delta\cos\theta.$$

Therefore, I_n defined by (2) becomes

$$I_n = \int_{-\pi}^{\pi}\int_{0}^{\pi} \frac{a^2\sin\theta}{(a^2+\delta^2-2a\delta\cos\theta)^n} d\theta d\phi = 2\pi a^2 \int_0^{\pi} \frac{\sin\theta}{(a^2+\delta^2-2a\delta\cos\theta)^n} d\theta.$$

By substituting $t = a^2 + \delta^2 - 2a\delta\cos\theta$, we have

$$I_n = \frac{\pi a}{\delta}\int_{(a-\delta)^2}^{(a+\delta)^2} t^{-n} dt = \frac{\pi a}{\delta(n-1)}\left[\frac{1}{(\delta-a)^{2n-2}} - \frac{1}{(\delta+a)^{2n-2}}\right]. \tag{3}$$

For $n = 3$ and $n = 6$, we may deduce

$$\begin{aligned} I_3 =& \frac{\pi a}{2\delta}\left[\frac{1}{(\delta-a)^4} - \frac{1}{(\delta+a)^4}\right], \\ I_6 =& \frac{\pi a}{5\delta}\left[\frac{1}{(\delta-a)^{10}} - \frac{1}{(\delta+a)^{10}}\right]. \end{aligned}$$

Next the atom will be assumed to be an arbitrary point on the surface of CeO_2 nanoparticles. Consequently, a second surface integration is necessary to calculate the total interaction energy of the system. Our goal is to

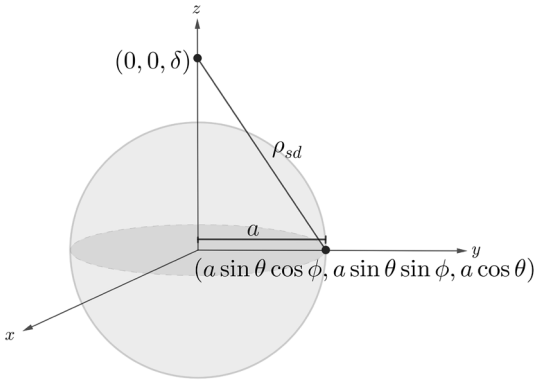

Fig. 4. Schematic model for atom located at $(0, 0, \delta)$ interacting with sphere of radius a centered at origin.

determine the distance between the DOX molecule and the CeO_2 structures and then perform another surface integral. Specifically, we rewrite I_3 and I_6 as a difference of squares, $\delta^2 - a^2$. The expressions for these are

$$I_3 = 4\pi a^2 \left[\frac{1}{(\delta^2 - a^2)^3} + \frac{2a^2}{(\delta^2 - a^2)^4} \right], \tag{4}$$

$$I_6 = \frac{4\pi a^2}{5} \left[\frac{5}{(\delta^2 - a^2)^6} + \frac{80a^2}{(\delta^2 - a^2)^7} + \frac{336a^4}{(\delta^2 - a^2)^8} + \frac{512a^6}{(\delta^2 - a^2)^9} + \frac{256a^8}{(\delta^2 - a^2)^{10}} \right]. \tag{5}$$

To further extend this analysis, we introduce another integral J_m defined by

$$J_m = \int_{S_2} \frac{1}{(\delta^2 - a^2)^m} dS_2, \tag{6}$$

where m is an integer exponent in equations (5) and (4). Consequently, equations (5) and (4) can be expressed in the form

$$I_3 = 4\pi a^2 (J_3 + 2a^2 J_4),$$
$$I_6 = \frac{4\pi a^2}{5} (5J_6 + 80a^2 J_7 + 336a^4 J_8 + 512a^6 J_9 + 256a^8 J_{10}).$$

For the full, step-by-step derivations and detailed integral manipulations necessary to reach the closed-form expressions presented in this section, readers are kindly directed to our published work[39].

In the following sections, we will evaluate the interaction energy between the spherical DOX molecule and three different shapes of CeO_2 nanostructures. The schematic models for these are presented in Fig. 5. The CeO_2 structures are assumed to be centered at the origin, while the center of the DOX molecule is shifted along the z-direction by a distance d. The parameter δ, as shown in equations (3) and (6), now represents the Euclidean distance from the center of the DOX molecule to a surface element on the CeO_2 structure. Our primary objective is to determine the minimum total energy of the system by treating the total energy as a function of the inter-spacing ξ, which is defined as the shortest distance between the surface of the spherical DOX and the surface of the CeO_2 nanostructure.

Spherical DOX interacting with spherical CeO_2

We assume the spherical CeO_2 nanoparticle has a radius of b_1, as shown in Fig. 5(a). Note that when $b_1 < d$, the DOX molecule is located on the surface of the CeO_2 nanoparticle, while when $b_1 > d$, the drug molecule is encapsulated inside it. The squared distance between the center of the DOX molecule and a surface element on the CeO_2 nanoparticle is given by

$$\begin{aligned} \delta^2 =& (b_1 \sin\theta \cos\phi)^2 + (b_1 \sin\theta \sin\phi)^2 + (b_1 \cos\theta - d)^2 \\ =& b_1^2 + d^2 - 2b_1 d \cos\theta. \end{aligned}$$

The integral I_n given in (3) may be deduced

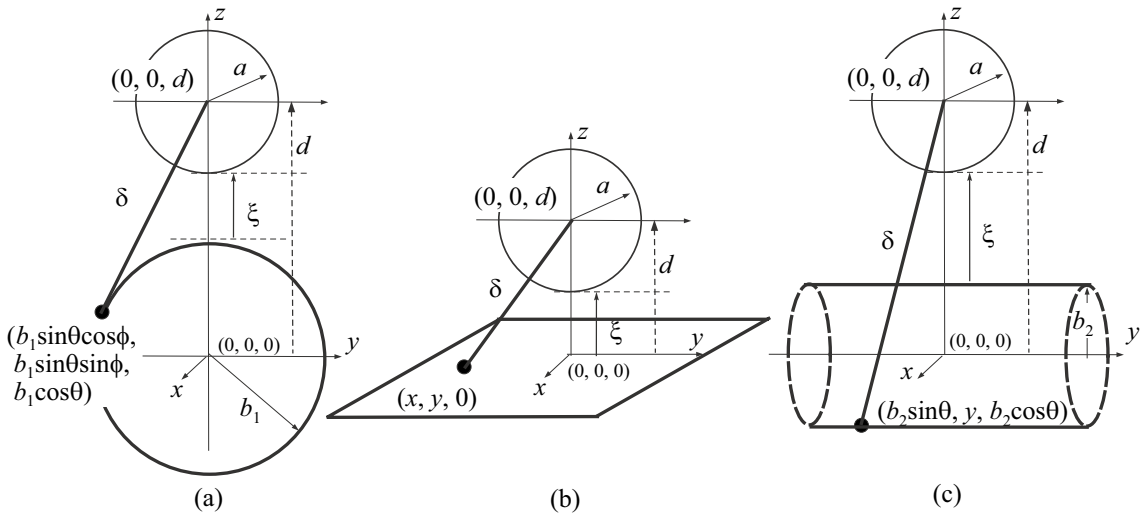

Fig. 5. Schematic models for spherical DOX molecule interacting with (**a**) spherical, (**b**) planar and (**c**) cylindrical shapes of CeO_2 nanoparticles.

$$I_{ns} = \frac{\pi a}{(n-1)} \int_{-\pi}^{\pi} \int_{0}^{\pi} \frac{b_1^2 \sin\theta}{\delta} \left[\frac{1}{(\delta - a)^{2n-2}} - \frac{1}{(\delta + a)^{2n-2}} \right] d\theta d\phi$$
$$= \frac{2\pi^2 a}{(n-1)} \int_{0}^{\pi} \frac{b_1^2 \sin\theta}{\delta} \left[\frac{1}{(\delta - a)^{2n-2}} - \frac{1}{(\delta + a)^{2n-2}} \right] d\theta,$$

where we define the integral to be I_{ns} for the second surface element of another sphere. As there is no dependence on ϕ in the integrand, this can be done immediately and then we make the substitution of δ for θ, which yields

$$\begin{aligned} I_{ns} &= \frac{2\pi^2 a b_1}{(n-1)} \int_{(d-b_1)}^{(d+b_1)} \left[\frac{1}{(\delta - a)^{2n-2}} - \frac{1}{(\delta + a)^{2n-2}} \right] d\delta \\ &= \frac{2\pi^2 a b_1}{d(n-1)(2n-3)} \left[\frac{1}{(d - b_1 - a)^{2n-3}} - \frac{1}{(d + b_1 - a)^{2n-3}} - \frac{1}{(d - b_1 + a)^{2n-3}} + \frac{1}{(d + b_1 + a)^{2n-3}} \right]. \end{aligned} \tag{7}$$

Therefore, the total interaction energy between two spherical molecules is given by

$$E_S = \eta_1 \eta_2 \left(-A I_{3s} + B I_{6s} \right), \tag{8}$$

where I_{ns} for $n = 3$ and 6 are defined by (7).

Spherical DOX interacting with planar sheet of CeO_2

As illustrated in Fig. 5(b), the squared distance from the center of the DOX molecule to a point on the *xy*-plane is given by $\delta^2 = x^2 + y^2 + d^2$. Due to the short-range nature of the vdW force with the cut-off distance $0.1 - 1.0$ nm[40], the CeO_2 sheet can be approximated as an infinite flat plane. Utilizing the integral J_m defined in equation (6), we introduce J_{mp} to represent the contribution from the second surface element, which is an infinite plane. This allows us to deduce

$$J_{mp} = \int_{-\infty}^{\infty} \int_{-\infty}^{\infty} (x^2 + y^2 + d^2 - a^2)^{-m} dx dy.$$

We then make a change of variable substitution of $x = \sqrt{y^2 + d^2 - a^2} \tan^2 \psi$ which transforms the integral to

$$J_{mp} = \int_{-\infty}^{\infty} (y^2 + d^2 - a^2)^{1/2-m} \int_{-\pi/2}^{\pi/2} \cos^{2m-2} \psi d\psi dy.$$

By using an integral definition of the beta function, which is

$$\int_{0}^{\pi/2} \sin^p \theta \cos^q \theta d\theta = \frac{1}{2} B\left(\frac{p+1}{2}, \frac{q+1}{2} \right),$$

and $B(x, y) = B(y, x)$, yields

$$J_{mp} = B\left(m - \frac{1}{2}, \frac{1}{2} \right) \int_{-\infty}^{\infty} (y^2 + d^2 - a^2)^{1/2-m} dy.$$

We repeat this process for the substitution of *y*, finally we have

$$J_{mp} = B\left(m - \frac{1}{2}, \frac{1}{2} \right) B\left(m - 1, \frac{1}{2} \right) \frac{1}{(d^2 - a^2)^{m-1}}. \tag{9}$$

The analytical expression for the total interaction energy between a sphere of radius *a* and a planar sheet is

$$E_P = 4\pi a^2 \eta_1 \eta_2 \left[-A(J_{3p} + 2a^2 J_{4p}) + \frac{B}{5}(5J_{6p} + 80a^2 J_{7p} + 336a^4 J_{8p} + 512a^6 J_{9p} + 256a^8 J_{10p}) \right], \tag{10}$$

where J_{mp} for integers *m* are given by (9).

Spherical DOX interacting with cylindrical CeO_2

This section evaluates the interaction energy between a sphere and an infinite cylindrical surface with a radius of b_2. The infinite body assumption is an acceptable simplification given the short-range nature of the vdW force and is necessary to maintain analytical tractability. A schematic of this model is presented in Fig. 5(c). As with the spherical model, the location of the DOX molecule, whether it is inside or outside the nanoparticle, can be determined by the relationship between the cylinder's radius b_2 and the vertical distance *d*. The squared distance from the center of the sphere to any arbitrary surface element on the cylinder is expressed as

$$\delta^2 = (b_2 \sin\theta)^2 + y^2 + (b_2 \cos\theta - d)^2 = (d - b_2)^2 + 4 b_2 d \sin^2(\theta/2) + y^2,$$

where we utilized the identity $1-\cos\theta = 2\sin^2(\theta/2)$. Given that vdW forces are short-range, we model the cylinder as an infinite surface and integrate over its entire length y from $-\infty$ to ∞. This simplification is valid because the contribution to the total energy from the cylindrical ends is assumed to be negligibly small.

Based on the expression for the integral J_m given in equation (6), we introduce the term J_{mc} to represent the contribution from the second surface element, which is an infinite cylinder, and this allows us to deduce

$$J_{mc} = \int_{-\pi}^{\pi}\int_{-\infty}^{\infty} \frac{b_2}{[(d-b_2)^2 + 4b_2 d\sin^2(\theta/2) + y^2 - a^2]^m} dy d\theta.$$

We define $\lambda^2 = (d-b_2)^2 + 4b_2 d\sin^2(\theta/2) - a^2$, and make a substitution $y = \lambda\tan\psi$ to obtain

$$J_{mc} = b_2 \int_{-\pi}^{\pi} \lambda^{1-2m} \int_{-\pi/2}^{\pi/2} \cos^{2m-2}\psi d\psi d\theta.$$

Again, we use the integral definition for beta function, and use the face that λ is an even function in terms of θ, we have

$$J_{mc} = 2b_2 B\left(m-\frac{1}{2},\frac{1}{2}\right)\int_0^{\pi} \frac{1}{\lambda^{2m-1}} d\theta.$$

By introducing the variable $t = \sin^2(\theta/2)$, the expression is transformed into

$$J_{mc} = \frac{2b_2}{[(d-b_2)^2 - a^2]^{m-1/2}} B\left(m-\frac{1}{2},\frac{1}{2}\right)\int_0^1 t^{-1/2}(1-t)^{-1/2}(1-\mu t)^{1/2-m} dt,$$

where $\mu = -4b_2 d/[(d-b_2)^2 - a^2]$. The above integral is in the Euler form of the hypergeometric function

$$F(a,b;c;z) = \frac{\Gamma(c)}{\Gamma(b)\Gamma(c-b)}\int_0^1 t^{b-1}(1-t)^{c-b-1}(1-zt)^{-a} dt,$$

and $\Gamma(x)$ is a gamma function. Then we have

$$J_{mc} = \frac{2\pi b_2}{[(d-b_2)^2 - a^2]^{m-1/2}} B\left(m-\frac{1}{2},\frac{1}{2}\right) F\left(m-\frac{1}{2},\frac{1}{2};1;-\frac{4b_2 d}{(d-b_2)^2 - a^2}\right), \tag{11}$$

where $\frac{\Gamma(1/2)\Gamma(1/2)}{\Gamma(1)} = \pi$. The final analytical expression for the total interaction energy between a sphere of radius a and an infinite cylinder of radius b_2 is

$$E_C = 4\pi a^2 \eta_1\eta_2\left[-A(J_{3c} + 2a^2 J_{4c}) + \frac{B}{5}(5J_{6c} + 80a^2 J_{7c} + 336a^4 J_{8c} + 512a^6 J_{9c} + 256a^8 J_{10c})\right], \tag{12}$$

where J_{mc} for integers m are given by (11).

Numerical results

In this study, DOX molecule is modeled as a sphere with a radius of 0.75 nm as reported in[41]. We utilize a mean atomic surface density of $\eta_{DOXs} = 1.1922 \times 10^{-2}$ nm^{-2}, an optimal value determined from U-NSGA-III simulations of the DOX-graphene interaction that yielded a calculated energy of -51.4158 kcal/mol[42]. For the CeO_2 nanoparticles, we calculate the mean atomic surface density using the formula for tessellated hexagonal rings, given by

$$\eta = \frac{4\sqrt{3}}{9\sigma^2},$$

where σ represents the bond length. With a CeO_2 bond length of $\sigma_{Ce} = 0.209$ nm, the mean surface density is calculated to be $\eta_{Ce} = 1.762 \times 10^{-3}$ nm^{-2}. This value is consistently applied to all three CeO_2 nanoparticle structures examined in this study.

To validate our analytical expressions for a spherical DOX interacting with spherical, planar sheet, and cylindrical CeO_2 nanoparticles, we consider two distinct scenarios, the DOX molecule is either inside the nanoparticle or on its surface. The specific expressions used for the spherical, sheet, and cylindrical interactions are provided in equations (8), (10), and (12), respectively. We model the spherical and cylindrical CeO_2 nanoparticles with a radius of 20 nm, a size large enough to capture the full vdW energy of the system[40]. The resulting energy profiles as a function of the inter-spacing ξ are presented in Fig. 6. In this figure, a negative value of ξ (dashed lines) indicates the DOX molecule is inside the nanoparticle, while a positive value (solid lines) shows it is on the surface. The numerical values for the inter-spacing ξ at which these energy minima occur are reported in Table 3.

When a DOX molecule is encapsulated inside the nanoparticles, the spherical CeO_2 configuration results in the lowest minimum energy, indicating the most stable system among the three geometries. Conversely, the

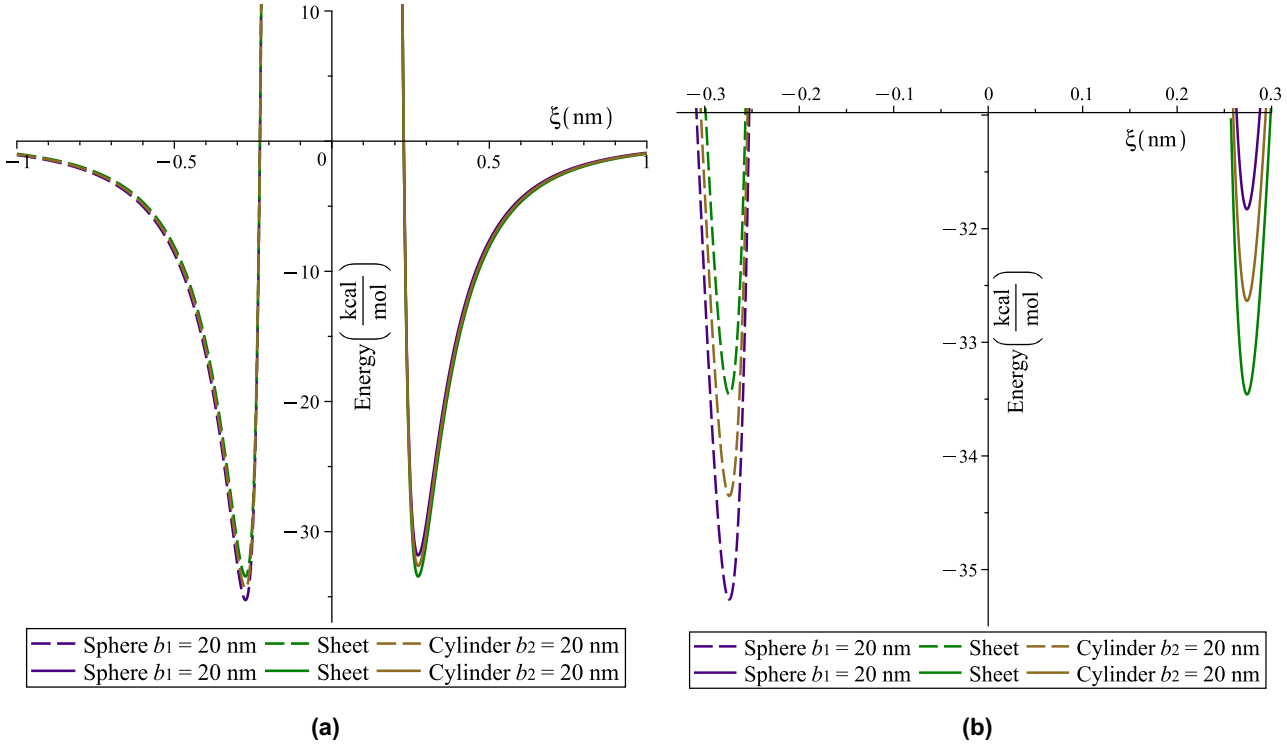

Fig. 6. Interaction energy profiles for DOX sphere of radius $a = 0.75$ nm and various CeO_2 nanoparticle geometries. The energy is plotted as a function of inter-particle spacing ξ. Dashed lines correspond to DOX being located inside CeO_2 ($\xi < 0$), while solid lines indicate its position on the surface ($\xi > 0$). Both the spherical and cylindrical CeO_2 are modeled with radius of 20 nm. (**a**) Full range of attractive and repulsive forces and (**b**) zoomed view of the attractive equilibrium.

	DOX inside		DOX on surface	
CeO_2 NPs	E_{min}	$\|\xi\|$	E_{min}	ξ
Sphere	−35.2641	0.2742	−31.8289	0.2739
Sheet	−33.4585	0.2740	−33.4585	0.2740
Cylinder	−34.3521	0.2741	−32.6358	0.2740

Table 3. Minimum interaction energy E_{min} (kcal/mol) and corresponding inter-spacing ξ (nm) for spherical DOX ($a = 0.75$ nm) interacting with various CeO_2 nanoparticle shapes (sphere, sheet, and cylinder). Results are presented for local energy minima found both inside and on the surface of the nanoparticles. The spherical and cylindrical nanoparticles are assumed to have a radius of 20 nm.

planar sheet geometry yields the highest energy at equilibrium. This difference in stability is attributed to the optimal curvature matching between the inner spherical surface of the DOX molecule and the outer spherical CeO_2 nanoparticle.

The order of stability changes for DOX molecules adsorbed on the surface of the nanoparticles. In this case, the lowest minimum energy is observed for the interaction with the CeO_2 sheet, while the highest energy occurs with the spherical CeO_2. It is important to note that despite these differences, the minimum energy values for all six scenarios are very close, suggesting a similar binding energy behavior across all three geometries.

Based on our experimental loading efficiency data presented in Table 1, the C-sphere-DOX system exhibited the highest efficiency, followed by C-cylinder-DOX and then C-sheet-DOX. This experimental order of stability mirrors the theoretical calculation for the loading of the drug inside the nanoparticles. The strong agreement between the experimental results and the theoretical predictions for loading suggests that the final location of the DOX molecule in our experiment is likely a combination of both encapsulated and surface-adsorbed states.

Furthermore, as shown in Fig. 6, the binding energy is consistently stronger when the drug is encapsulated inside the nanoparticles than when it is on the surface. This suggests that the encapsulated state is more stable and thus advantageous for drug storage and loading. The lower binding energy on the nanoparticle surface, in contrast, is favorable for a sustained drug release mechanism.

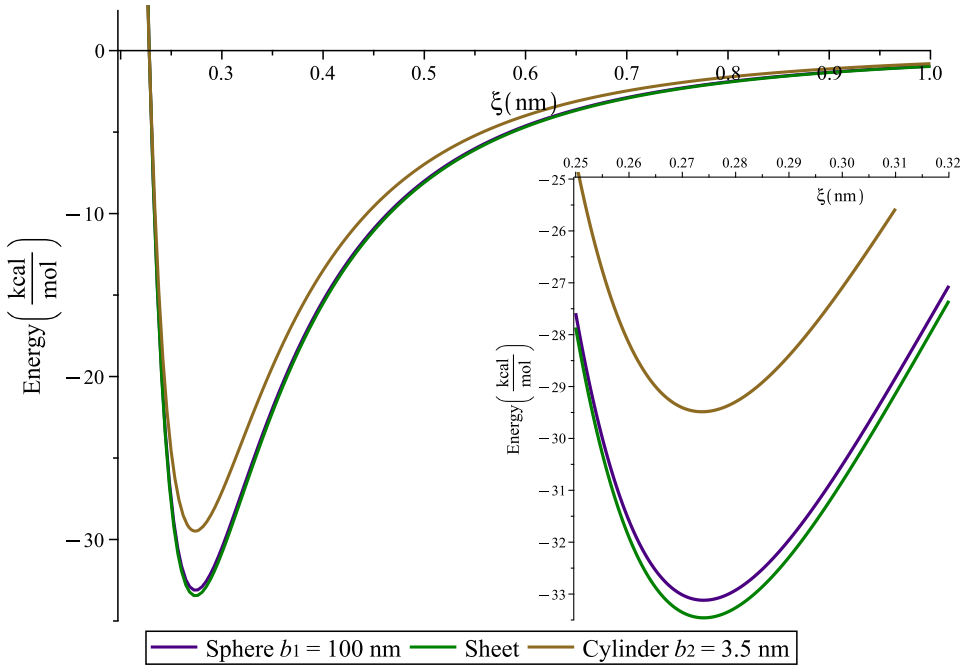

Fig. 7. Energy profiles for DOX of radius $a = 0.75$ nm adsorption on surface of spherical, sheet, and cylindrical CeO_2 nanoparticles. The adsorption energy is shown as a function of separation distance ξ, and the inset provides a zoomed-in view of minimum energy locations.

For all cases, the equilibrium inter-spacing ξ is found to be a similar value of approximately 0.274 nm. A notable symmetric behavior is observed for the planar sheet geometry. Due to its infinite nature, the loading of the DOX molecule (on one side of the sheet) and its absorption on the surface (on the other side) yield identical energy values and equilibrium distances.

Despite the assumption of infinite size for the sheet and cylindrical geometries in our analytical model, we applied these mathematical expressions to validate the corresponding experimental findings. Based on the nanoparticle sizes detailed in Section 2.3, we used a radius of 100 nm for the spherical CeO_2 and 3.5 nm for the cylindrical CeO_2. Assuming the DOX molecules are on the nanoparticle surfaces, we plotted the energy as a function of the positive inter-spacing ξ as shown in Fig. 7. We observed that the spherical and sheet geometries yielded very close binding energy values at equilibrium, specifically 33.1193 and 33.4585 kcal/mol, respectively. In contrast, the cylindrical shape produced a lower binding energy of 29.4859 kcal/mol. However, this theoretical result for the cylindrical shape differs from the experimentally measured loading efficiency presented in Table 1. This discrepancy may be attributed to a limitation of our current mathematical model, which neglects the influence of the surrounding media and its associated effects on the vdW forces and overall molecular interaction.

The use of a vacuum-based model is methodologically justified for predicting the geometric trend. In a relative comparison of the DOX/Sphere, DOX/Sheet, and DOX/Cylinder binding energies, the inherent complexities of the solvent-mediated forces, specifically the common DOX/Solvent and CeO_2/Solvent interaction energy terms are assumed to effectively cancel. This strategic cancellation allows the simpler model to precisely isolate and quantify the pure effect of surface curvature and geometry on the vdW interaction.

Summary

In this study, we employed a combined experimental and analytical approach to investigate the fundamental interaction between a spherical doxorubicin (DOX) molecule and three distinct CeO_2 nanoparticle geometries, spherical, planar sheet, and cylindrical. Our primary goal was to understand how nanoparticle shape influences drug loading efficiency.

Analytically, we developed closed-form mathematical models to determine the van der Waals (vdW) interaction energy. The models considered two geometric scenarios—DOX loaded within the nanoparticles and DOX adsorbed on their surface. Our calculations revealed that the spherical CeO_2 system yielded the lowest minimum energy for the loading scenario, while the sheet geometry provided the most stable interaction for surface adsorption. However, across all geometries and scenarios, the minimum energy values were remarkably close, indicating a similar initial binding tendency.

In the experimental phase, the three distinct CeO_2 shapes were synthesized, characterized, and their respective DOX loading efficiencies and cytotoxicity toward breast cancer cells were measured. Applying our analytical models—which assume an infinite dimension but were corrected using actual TEM-obtained nanoparticle dimensions—a strong alignment between theory and experiment was observed, the model successfully predicted similar and high relative thermodynamic stability for the spherical and sheet geometries.

Crucially, a significant quantitative discrepancy arose with the cylindrical shape, where the model's predicted low binding energy did not correspond to the exceptionally high experimentally determined loading efficiency. This divergence highlights two key limitations in the current analytical framework, (i) the neglect of the surrounding solvent effects on the vdW interaction, and (ii) the simplifying assumption of a singular, uniform mean atomic surface density across all three CeO_2 morphologies, which ignores actual crystallographic variations (e.g., exposed facets).

In summary, the synergy of these two methods provides a rigorous foundation by establishing the vdW model as a reliable tool for predicting the initial geometric binding tendency. However, the observed failure to quantitatively predict the exceptional loading of the cylindrical CeO_2 serves as our most important finding, mandating a new research direction. Future computational efforts must move beyond idealized vacuum conditions to incorporate the full complexity of the nano-bio interface, specifically Lifshitz theory for solvent effects and multi-site modeling for aggregation, to achieve true quantitative predictive power for complex nanomedicine systems.

Data availability

The datasets used and analysed during the current study available from the corresponding author on reasonable request.

Received: 7 October 2025; Accepted: 17 January 2026
Published online: 24 January 2026

References

1. Paluszkiewicz, P. et al. The application of nanoparticles in diagnosis and treatment of kidney diseases. *Int. J. Mol. Sci.* **23**, https://doi.org/10.3390/ijms23010131 (2022).
2. Xu, H., Li, S. & Liu, Y.-S. Nanoparticles in the diagnosis and treatment of vascular aging and related diseases. *Signal Transduct. Target. Ther.* **7**, 231. https://doi.org/10.1038/s41392-022-01082-z (2022).
3. Wang, B. et al. Current advance of nanotechnology in diagnosis and treatment for malignant tumors. *Signal Transduct. Target. Ther.* **9**, 200. https://doi.org/10.1038/s41392-024-01889-y (2024).
4. Puttasiddaiah, R. et al. Emerging nanoparticle-based diagnostics and therapeutics for cancer: Innovations and challenges. *Pharmaceutics* **17**, https://doi.org/10.3390/pharmaceutics17010070 (2025).
5. Prapainop, K., Miao, R., Åberg, C., Salvati, A. & Dawson, K. A. Reciprocal upregulation of scavenger receptors complicates interpretation of nanoparticle uptake in non-phagocytic cells. *Nanoscale* **9**, 11261–11268. https://doi.org/10.1039/C7NR03254D (2017).
6. Patra, J. K. et al. Nano based drug delivery systems: recent developments and future prospects. *J. Nanobiotechnology* **16**, 71. https://doi.org/10.1186/s12951-018-0392-8 (2018).
7. Mekseriwattana, W. et al. Dual functions of riboflavin-functionalized poly(lactic-co-glycolic acid) nanoparticles for enhanced drug delivery efficiency and photodynamic therapy in triple-negative breast cancer cells. *Photochem. Photobiol.* **97**, 1548–1557. https://doi.org/10.1111/php.13464 (2021).
8. Mekseriwattana, W. et al. Riboflavin–citrate conjugate multicore spions with enhanced magnetic responses and cellular uptake in breast cancer cells. *Nanoscale Adv.* **4**, 1988–1998. https://doi.org/10.1039/D2NA00015F (2022).
9. Afzal, O. et al. Nanoparticles in drug delivery: From history to therapeutic applications. *Nanomaterials* **12**, https://doi.org/10.3390/nano12244494 (2022).
10. Sultana, A., Zare, M., Thomas, V., Kumar, T. S. & Ramakrishna, S. Nano-based drug delivery systems: Conventional drug delivery routes, recent developments and future prospects. *Med. Drug Discov.* **15**, 100134. https://doi.org/10.1016/j.medidd.2022.100134 (2022).
11. Yusuf, A., Almotairy, A. R. Z., Henidi, H., Alshehri, O. Y. & Aldughaim, M. S. Nanoparticles as drug delivery systems: A review of the implication of nanoparticles' physicochemical properties on responses in biological systems. *Polymers* **15**, https://doi.org/10.3390/polym15071596 (2023).
12. Egwu, C. O. et al. Nanomaterials in drug delivery: Strengths and opportunities in medicine. *Molecules* **29**, https://doi.org/10.3390/molecules29112584 (2024).
13. Payomhom, P. et al. Chitosan-coated poly(lactic-co-glycolic acid) nanoparticles loaded with ursolic acid for breast cancer therapy. *ACS Appl. Nano Mater.* **7**, 5383–5395. https://doi.org/10.1021/acsanm.3c06161 (2024).
14. Xu, C. & Qu, X. Cerium oxide nanoparticle: a remarkably versatile rare earth nanomaterial for biological applications. *NPG Asia Mater.* **6**, e90–e90. https://doi.org/10.1038/am.2013.88 (2014).
15. Gavinho, S. R. et al. Biocompatibility, bioactivity, and antibacterial behaviour of cerium-containing bioglass®. *Nanomaterials* **12**, https://doi.org/10.3390/nano12244479 (2022).
16. Cheng, F. et al. Ceria nanoenzyme-based hydrogel with antiglycative and antioxidative performance for infected diabetic wound healing. *Small Methods* **6**, 2200949. https://doi.org/10.1002/smtd.202200949 (2022).
17. Asati, A., Santra, S., Kaittanis, C. & Manuel, P. J. Surface-charge-dependent cell localization and cytotoxicity of cerium oxide nanoparticles. *ACS Nano* **4**, 5321–5331. https://doi.org/10.1021/nn100816s (2010).
18. Pramanik, N. et al. Surface-coated cerium nanoparticles to improve chemotherapeutic delivery to tumor cells. *ACS Omega* **7**, https://doi.org/10.1021/acsomega.2c00062 (2022).
19. Mahdavi, M., Shahbazi, S., Reiisi, S. & Rigi, G. Investigating the cell proliferation and migration inhibition by cerium oxide nanoparticles loaded with doxorubicin in mda-mb-231 cell line. *Nanomed. J.* **11**, 426–437. https://doi.org/10.22038/nmj.2024.74952.1820 (2024).
20. Di Francesco, M. et al. Doxorubicin hydrochloride-loaded nonionic surfactant vesicles to treat metastatic and non-metastatic breast cancer. *ACS Omega* **6**, 2973–2989. https://doi.org/10.1021/acsomega.0c05350 (2021).
21. Yao, Y., Gao, X. & Zhou, Z. The application of drug loading and drug release characteristics of two-dimensional nanocarriers for targeted treatment of leukemia. *Front. Mater.* **Volume 10 - 2023**, https://doi.org/10.3389/fmats.2023.1209186 (2023).
22. Lisitsyna, E. S. et al. Fluorescence anisotropy for detailed analysis of doxorubicin loading into dna origami nanocarriers for drug delivery. *ACS Appl. Nano Mater.* **8**, 13274–13284. https://doi.org/10.1021/acsanm.5c01518 (2025).
23. Liu, Y., Tan, J., Thomas, A., Ou-Yang, D. & Muzykantov, V. R. The shape of things to come: Importance of design in nanotechnology for drug delivery. *Ther. Deliv.* **3**, 181–194. https://doi.org/10.4155/tde.11.156 (2012) (**PMID: 22834196**).
24. Öztürk, K., Kaplan, M. & Çalış, S. Effects of nanoparticle size, shape, and zeta potential on drug delivery. *Int. J. Pharm.* **666**, 124799. https://doi.org/10.1016/j.ijpharm.2024.124799 (2024).
25. Liu, W. et al. Rod-like mesoporous silica nanoparticles facilitate oral drug delivery via enhanced permeation and retention effect in mucus. *Nano Res.* **15**, 9243–9252. https://doi.org/10.1007/s12274-022-4601-2 (2022).

26. Ridolfo, R., Arends, J. J., van Hest, J. C. M. & Williams, D. S. Wormlike nanovector with enhanced drug loading using blends of biodegradable block copolymers. *Biomacromolecules* **21**, 2199–2207. https://doi.org/10.1021/acs.biomac.0c00169 (2020).
27. Zhou, K., Liu, B., Cai, Y., Dmitriev, S. V. & Li, S. Modelling of low-dimensional functional nanomaterials. *physica status solidi (RRL) - Rapid Research Letters* **16**, 2100654. https://doi.org/10.1002/pssr.202100654 (2022).
28. Celis, J. & Cao, W. Systematic dft modeling van der waals heterostructures from a complete configurational basis applied to γ-pc/ws2. *J. Chem. Theory Comput.* **20**, 2377–2389. https://doi.org/10.1021/acs.jctc.3c00932 (2024).
29. Grimme, S. & Schreiner, P. R. The role of london dispersion interactions in modern chemistry. *Acc. Chem. Res.* **57**, 2233–2233. https://doi.org/10.1021/acs.accounts.4c00465 (2024).
30. Richfield, O., Piotrowski-Daspit, A. S., Shin, K. & Saltzman, W. M. Rational nanoparticle design: Optimization using insights from experiments and mathematical models. *J. Control. Release* **360**, 772–783. https://doi.org/10.1016/j.jconrel.2023.07.018 (2023).
31. Sumetpipat, K. & Baowan, D. Three model shapes of doxorubicin for liposome encapsulation. *J. Mol. Model.* **20**, 2504. https://doi.org/10.1007/s00894-014-2504-1 (2014).
32. Putthikorn, S. & Baowan, D. Mathematical model for drug molecules encapsulated in lipid nanotube. *Phys. A: Stat. Mech. Appl.* **461**, 46–60. https://doi.org/10.1016/j.physa.2016.05.027 (2016).
33. Putthikorn, S., Ruengrot, P. & Baowan, D. Energy behaviour of doxorubicin interacting with peptide nanotubes. *J. Math. Chem.* **58**, 382–392. https://doi.org/10.1007/s10910-019-01087-0 (2020).
34. Jiang, P. et al. Tuning oxidant and antioxidant activities of ceria by anchoring copper single-site for antibacterial application. *Nat. Commun.* **15**, 1010. https://doi.org/10.1038/s41467-024-45255-6 (2024).
35. Mai, H.-X. et al. Shape-selective synthesis and oxygen storage behavior of ceria nanopolyhedra, nanorods, and nanocubes. *J. Phys. Chem. B* **109**, 24380–24385. https://doi.org/10.1021/jp055584b (2005).
36. Iqbal, N. et al. Interrelationships between the structural, spectroscopic, and antibacterial properties of nanoscale ($<$ 50 nm) cerium oxides. *Sci. Rep.* **11**, 20875. https://doi.org/10.1038/s41598-021-00222-9 (2021).
37. Armbruster, D. A. & Pry, T. Limit of blank, limit of detection and limit of quantitation. *Clin. Biochem. Rev.* **29**(Suppl 1), S49-52 (2008).
38. Rapp$\acute{e}$, A. K., Casewit, C. J., Colwell, K. S., Goddard III, W. A. & Skiff, W. M. UFF, a full periodic table force field for molecular mechanics and molecular dynamics simulations. *J. Am. Chem. Soc.* **114**, 10024–10035, https://doi.org/10.1021/ja00051a040 (1992).
39. Baowan, D., Cox, B. J., Hilder, T. A., Hill, J. M. & Thamwattana, N. *Modelling and Mechanics of Carbon-based Nanostructured Materials* (William Andrew, 2017).
40. Abbasfard, H., Evans, G. & Moreno-Atanasio, R. Effect of van der waals force cut-off distance on adhesive collision parameters in dem simulation. *Powder Technol.* **299**, 9–18. https://doi.org/10.1016/j.powtec.2016.05.020 (2016).
41. Bilalis, P., Tziveleka, L.-A., Varlas, S. & Iatrou, H. ph-sensitive nanogates based on poly(l-histidine) for controlled drug release from mesoporous silica nanoparticles. *Polym. Chem.* **7**, 1475–1485. https://doi.org/10.1039/C5PY01841B (2016).
42. Sumetpipat, K. & Baowan, D. Stable configurations of DOXH interacting with graphene: Heuristic algorithm approach using NSGA-II and U-NSGA-III. *Nanomaterials* **12**, 4097. https://doi.org/10.3390/nano12224097 (2022).

Acknowledgements

S.K. was thankful for the Graduate Research Assistantship (RA) scholarship for financial aid to support education and research of a graduate student, Faculty of Graduate Studies, Mahidol University. A.W. was supported by a Postdoctoral fellowship award from Mahidol University. P.L would like to thank the Kasetsart University Research Development Institute (KURDI).

Author contributions

K.K. and D.B. designed the study. S.K., A.W. and K.K. conducted the experiments. W.S., N.T. and P.L. prepared the experimental materials. P.S. and D.B. performed the analytical calculations. All authors wrote, reviewed and edited the manuscript.

Funding

This research project has been supported by Mahidol University (Fundamental Fund: fiscal year 2025 by National Science Research and Innovation Fund (NSRF) (FF-068/2568). Partial support was also provided by a grant from the Center for Scientific Instrumentation and Platform Services, Faculty of Science, Mahidol University.

Declarations

Competing interests

The authors declare no competing interests.

Additional information

Supplementary Information The online version contains supplementary material available at https://doi.org/10.1038/s41598-026-36893-5.

Correspondence and requests for materials should be addressed to K.K. or D.B.

Reprints and permissions information is available at www.nature.com/reprints.

Publisher's note Springer Nature remains neutral with regard to jurisdictional claims in published maps and institutional affiliations.

Open Access This article is licensed under a Creative Commons Attribution-NonCommercial-NoDerivatives 4.0 International License, which permits any non-commercial use, sharing, distribution and reproduction in any medium or format, as long as you give appropriate credit to the original author(s) and the source, provide a link to the Creative Commons licence, and indicate if you modified the licensed material. You do not have permission under this licence to share adapted material derived from this article or parts of it. The images or other third party material in this article are included in the article's Creative Commons licence, unless indicated otherwise in a credit line to the material. If material is not included in the article's Creative Commons licence and your intended use is not permitted by statutory regulation or exceeds the permitted use, you will need to obtain permission directly from the copyright holder. To view a copy of this licence, visit http://creativecommons.org/licenses/by-nc-nd/4.0/.

© The Author(s) 2026